Piezo-photoelectronic coupling effect of $BaTiO_3$@TiO_2 nanowires for high concentrated dye degradation

Qiong Liu, Di Zhai, Zhida Xiao, Chen Tang, Qiwei Sun, Chris R Bowen, Hang Luo*, Dou Zhang*

State Key Laboratory of Powder Metallurgy, Central South University, Changsha, Hunan 410083, China.

*Corresponding author

E-mail address: dzhang@csu.edu.cn (Dou Zhang)

E-mail address: hangluo@csu.edu.cn (Hang Luo)

Abstract The induced built-in electric field by piezoelectric materials has proven to be one of the most effective strategies for modulating the charge-transfer pathway and inhibiting carrier recombination. In this work, a series of core-shell strucutred $BaTiO_3$@TiO_2 nanowires (BT@TiO_2 NWs) heterojunctions were synthesised and the significant coupling effects of $BaTiO_3$ (BT) and TiO_2 resulted in surperior piezo-photocatalytic performance, which was demonstrated by three typical types of dyes with high concentrations. The degradation efficiency of 30 mg/L Rhodamine B (RhB), Methylene blue (MB) and Indigo Carmine (IC) solutions by 0.5 g/L BT@TiO_2 NWs reached 99.5 % in 75 min, 99.8 % in 105 min and 99.7 % in 45 min, respectively, which are much higher than the piezo-photocatalysis records reported before. To reveal the coupling mechanisms, the photoelectrochemical measurements and band diagram analysis were carried out. The carrier concentration was increased from 2.28×10^{17} cm^{-3} to 4.91×10^{18} cm^{-3} and lifetime of charges was improved from 50.37 ms to 60.98 ms owning to the construction of heterojunction between TiO_2 and BT. It was proposed that the tilting and bending of the energy band caused by the introduction of piezoelectric polarization can facilitate carrier separation both in the bulk phase and at the surfaces of semiconductors, resulting in outstanding piezo-photocatalytic properties for highly concentrated dye degradation. This work provides a universal catalyzer for highly concentrated dye degradation.

Keywords: $BaTiO_3$@TiO_2 nanowires; Synergistic principle; Piezo-photocatalysis; Dye degradation

1. Introduction

In the past decades, photocatalysis has attracted intensive focus with many reports for environmental purification applications [1-4]. The inefficiency of charge separation within semiconductors remains a key factor that limits the performance of catalysts. Efforts have been made to provide a solution to this challenge, including impurity doping, the introduction of a co-catalyst and the construction of a heterojunction to improve the charge separation efficiency [5-8]. Piezoelectric-based catalysis is therefore now emerging as an advanced strategy [9-11]. While piezoelectricity is a well-known effect, where a piezoelectric material can generate an electrical potential under an applied mechanical stress, the induced built-in electric field can facilitate charge separation macroscopically for catalysis [12]. However, the direction of the internal electric field that is introduced by a piezoelectric materials has a significant impact for maximizing the enhancement of the photocatalytic activity. In our previous study, it was shown by simulation that when the junction structure of a piezoelectric and photoelectric materials is perpendicular to the built in electric field, the efficiency of charge separation of the photoelectric materials is at its the highest [13]. For zero dimensional piezoelectric materials, the probability of being subjected to the external force is equal for every part, and the direction of the internal electric field is therefore scattered. However, for one-dimensional piezoelectric materials, such as nanowires, the probability of external forces acting on the cylinder is greater than that on the two end surfaces. Therefore, the direction of the internal electric field tends to be perpendicular to the length direction of the nanowire, and adjusting the direction of the internal

electric field by using one-dimensional piezoelectric materials is beneficial to improve the photogenerated charge separation efficiency and catalytic performance.

$BaTiO_3$ is a typical lead-free piezoelectric material with a perovskite-type structure and has demonstated piezoelectric catalytic effect for the so-called "piezo-Fenton process" [14, 15]. H_2O_2 can be generated and facilely converted to •OH by BT due to its piezoelectric effect, where •OH is the active specie for dye degradation. In addition, BT has a bandgap of 3.2 eV and demonstrates a photoelectric performance due to its appropriate band position, which has been applied in water splitting and pollutant degradation. Yadav et al. reported that the salicylic acid was degraded by 51% in 120 min using a BT photocatalyst under ultraviolet illumination [16]. However, the catalytic performance of BT is remains general, and it can act as a piezoelectric catalyst or photoelectric catalyst. Titania (TiO_2) has been widely studied since 1972 and was demonstrated to exhibit the photocatalytic properties in water splliting by Fujishima A and Honda K [17]. However, due to the wide band gap of TiO_2, the narrow absorption range of light (only 3%) and the recombination of photogenerated electrons and holes, the photocatalytic performance of TiO_2 remains unsatisfactory [18-21].

In theory, a piezo/photo bi-catalystic heterojunction structure with BT and TiO_2 can effectively promote carrier separation and migration for matching the band energy [22, 23]. In addition, for BT@TiO_2 nanowires, the probability of a pressure acting on the cylinder is much greater than those acting on both end surfaces. The direction of the built-in electric field in the nanowire is mainly perpendicular to the direction of the BT nanowire. Therefore, a heterojunction constructed between BT and TiO_2 in a cylinder

can greatly promote charge separation when the major internal electric field is built up in a direction that is perpendicular to the direction of BT nanowire, which can greatly improve the piezo-photocatalytic performance for dye degradation.

In this work, BT nanowires (BT NWs) were synthesized through a two-step hydrothermal method and coated with anatase TiO_2 layers with different thicknesses in a chemical bath process to prepare the core-shell structured BT@TiO_2 NWs. The samples were defined as BT@TiO_2-40, BT@TiO_2-80 and BT@TiO_2-120, corresponding to different coating time of TiO_2 layers ranging from 40 to 120 min. Due to the construction of a heterojunction between TiO_2 and BT, the carrier concentration was increased from 2.28×10^{17} cm^{-3} to 4.91×10^{18} cm^{-3} and the lifetime of charges was improved from 50.37 ms to 60.98 ms. Furthermore, the built-in electric field generated by the internal polarization of BT facilitates the separation and migration of charge in the bulk phase, resulting in the improvement of effective charges for catalytic reaction. With a the coupling between photoelectric and piezoelectric effects, the BT@TiO_2 showed the almost highest rate constant as 0.207 min^{-1} for 5 mg/L RhB degradation. In addition, the degradation efficiency of 30 mg/L RhB, MB and IC solution with 0.5g/L BT@TiO_2-120 NWs reached 99.5 % in 75 min, 99.8 % in 105 min and 99.7 % in 45 min and the corresponding rate constant reached 0.067 min^{-1}, 0.047 min^{-1} and 0.108 min^{-1}, respectively, which demonstrated the outstanding piezo-photocatalytic properties for high concentrated dye degradation.

2. Experimental section

2.1. Chemical and reagents

All chemicals and reagents used in this study are analytical grade without further purification, including titanium dioxide (TiO_2, 99.98%, Sigma Aldrich), sodium hydroxide (NaOH, 99%, Sinopharm, China), barium hydroxide octahydrate ($Ba(OH)_2 \cdot 8H_2O$, 98%, Sinopharm, China), hydrochloric acid (HCl, 99%, Sinopharm, China), boric acid (H_3BO_3, 99.8%, Sinopharm, China), and ammonium hexafluorotitanate ($H_8F_6N_2Ti$, 99.8%, Sinopharm, China).

2.2. Synthesis of $BaTiO_3$ nanowires

$BaTiO_3$ nanowires (BT NWs) were synthesized by a two-step hydrothermal method. At first step, 1.25 g TiO_2 were added in 60 ml 10 M NaOH solution, stirred for 80 min and ultrasonicly vibrated for 35 min. The mixed solution was transferred into Teflon-lined autoclave and heated at 200 ℃ for 24 h. The products were washed with deionized water and anhydrous ethanol for three times, respectively. After drying at 70 °C, the resultant sodium titanate ($Na_2Ti_3O_7$) was stirred in dilute hydrochloric acid (HCl, 0.2 M) for 4 h at room temperature, followed by washing with deionized water and anhydrous ethanol respectively, until pH=7 of the solution was reached. Titanic acid ($H_2Ti_3O_7$) were obtained after drying at 70 ℃ for 12 h.

At the second step, 0.95 g barium hydroxide octahydrate ($Ba(OH)_2 \cdot 8H_2O$) were completely dissolved in 60 mL deionized water, and 0.15 g $H_2Ti_3O_7$ were added with ultrasonic vibration for 25 min. The mixed solution was transferred into Teflon-lined autoclave and heated at 200 ℃ for 8 h. The products were washed by deionized water and dried at 70 °C in an oven.

2.3. Synthesis of $BaTiO_3$@TiO_2 nanowires

BT@TiO_2 NWs were synthesized by a simple chemical bath method. 0.2 M boric acid (H_3BO_3) and 0.075 M ammonium fluorotanate ($H_8F_6N_2Ti$) were mixed in 100 mL deionized water and stirred until totally dissolved. The obtained BT NWs were added into the solution and stirred for 40, 80, and 120 min at 60 ℃, respectively. The products were washed with deionized water and anhydrous ethanol for three times respectively and then dried at 70 ℃ in an oven. Finally, the products were heated at 350 ℃ for 30 min at a rate of 1 ℃/min. The products were marked as BT@TiO_2-40, BT@TiO_2-80 and BT@TiO_2-120 respectively according to the chemical bath time.

2.4. Characterizations

X-ray diffractometer (XRD, D/Max 2250, λ=1.5418 Å, PANalytical Empyren, Netherlands) was applied to observe the phase structures of the samples. The morphologies and nanostructures were characterized by the scanning electron microscopy (SEM, Oxford x-max 20, tescan mira3) and transmission electron microscopy (TEM, Titan G2 60-300, USA), respectively. X-ray photoelectron spectrum (XPS) was conducted with an ESCALAB 250Xi spectrometer. The UV-Vis spectra of the materials were obtained with a spectrophotometer (PGeneral TU-1901). The UV-vis spectrophotometer (UV-2600i, Island ferry, Japan) was applied to detect the absorbance and diffuse reflection properties of dyes.

2.5. Catalytic performance test

The piezo-photocatalytic behaviors of the BT NWs and BT@TiO_2 NWs were measured by the decomposition of RhB, MB and IC dyes. The periodic mechanical

strain was provided by the ultrasonic machine (200 W, 45/80/100 kHz, KD-200, China). Light irradiation was applied with a Xe lamp (300 W, PLS-SXE300, China). Typically, 0.5 mg catalysts was dispersed in 100 ml dye aqueous solution with different initial concentration (eg. C_0 = 5, 10, 20, 30 mg/L), and stirred for 30 min to reach adsorption-desorption equilibrium between the dye and the catalysts, followed by treatment of sonication and/or illumination. 5 ml suspension was taken out for every 15 minutes and then centrifuged to obtain the supernatant. The dye absorbance and diffuse reflection was determined by the UV-vis spectrometer. Electron spin resonance (ESR) performances were test with the Bruker model A300 spectrometer (Bruker E500, Germany), and the 0.1 M 5, 5-dimethyl-1-pyrroline N-oxide (DMPO) was used as a spin trap. The ESR of RhB solution with or without 10 mL 0.1 g/L of BT@TiO_2-120 NWs and the pure DI water are carried out with light irradiation or/and ultrasonic vibration. 50 μL of the solution was immediately taken out and mixed with DMPO for detection.

2.6. Electrochemical measurements

Photoelectrochemical (PEC) performances of the samples were conducted on an electrochemical workstation (Chenhua CHI604E, Shanghai) with a typical three-electrode configuration. Photocurrent-potential (*J*-V) curves were obtained by linear sweeping voltammetry (LSV) with or without illumination at a scan rate of 20 mV s^{-1}. The platinum foil was used as counter electrode, the Ag/AgCl electrode (saturated KCl) was used as reference electrode, and the working electrodes were prepared as follows: 20 mg catalysts and 50 μL Nafion aqueous solution were dispersed in 2 ml ethyl alcohol

and ultrasonication for 30 min, followed by annealing at 200 °C for 3 h after being dropped onto the surface of FTO glass (2cm × 3cm). The illumination source was 300 W xenon lamp equipped with an AM 1.5 G filter to gain 1 sun illumination (100 mW cm^{-2}). The electrolyte was 0.5 M Na_2SO_4 (pH=7). In the experiment process, the working electrode was irradiated from the back side. The Mott-Schottky plots were measured at different frequency of 1 kHz, 2 kHz and 3 kHz without sonication and illumination, respectively. Electrochemical impedance spectroscopy (EIS) was measured under potential of 0.6 V (vs. Ag/AgCl), with an alternating voltage perturbation of 10 mV, while the AC frequency was set from 10 kHz to 0.1 Hz.

3. Results and discussion

3.1. Morphology and structure characterizations

Fig. 1a shows the flow chart of synthesis of BT, and Fig. 1b-f shows the XRD and SEM patterns of the pure BT and BT@TiO_2 samples. In Fig. 1b, the tetragonal phase structure of BT can be detected and the diffraction peaks at 22.1 °, 31.5 °, 38.8 °, 45.2 °, 56.2 ° and 65.7 ° are corresponding to the crystal faces of (100), (101), (111), (200), (211) and (202) of $BaTiO_3$ (PDF#81-2203), respectively. A weak peak near 24° relates to $BaCO_3$ impurities which is generated by the reaction of the $Ba(OH)_2 \cdot 8H_2O$ and CO_2 in air. After being coated with TiO_2, the impurity peak of the composite near 24° is eliminated. During the chemical bath treatment, the solution mixed with boric acid and ammonium fluorotanate is weakly acidic. $BaCO_3$ has therefore reacted with H^+ in the solution and dissolved. In addition, a new diffraction peak appears near 25.2 ° (marked

with the "◆" in Fig. 1b), which is consistent with the characteristic peak of anatase TiO_2 (PDF#83-2243). With an increase of the chemical bath time, the diffraction intensity of 25.2 ° becomes stronger, which is caused by the increase in the amount of TiO_2 coated on the BT. No other obvious impurity peak is observed for the composite material and the sharp diffraction peaks indicate the high crystallinity. As shown in Fig. 1c, pure BT NWs possesses the relatively uniform BT nanowires with diameter of ca. 200 nm and length over 2 μm. The surface of the nanowires is smooth, and the shape is a like a 'pod'. As Fig. 1d-f shows, after the in-situ crystallization of TiO_2 on BT NWs, the size of the nanowires become larger with the increased chamical bath time. In Fig. 1d, the diameter of the nanowires has no obvious change compared with Fig. 1c. When the chemical bath time is increased to 80 min (Fig. 1e) and 120 min (Fig. 1f), the diameter of the BT nanowire has changed markedly, and a concave-convex morphology of the pod-shape is obviously weakened. The surface of the nanowire is roughened after being decorated with layers of TiO_2 particles.

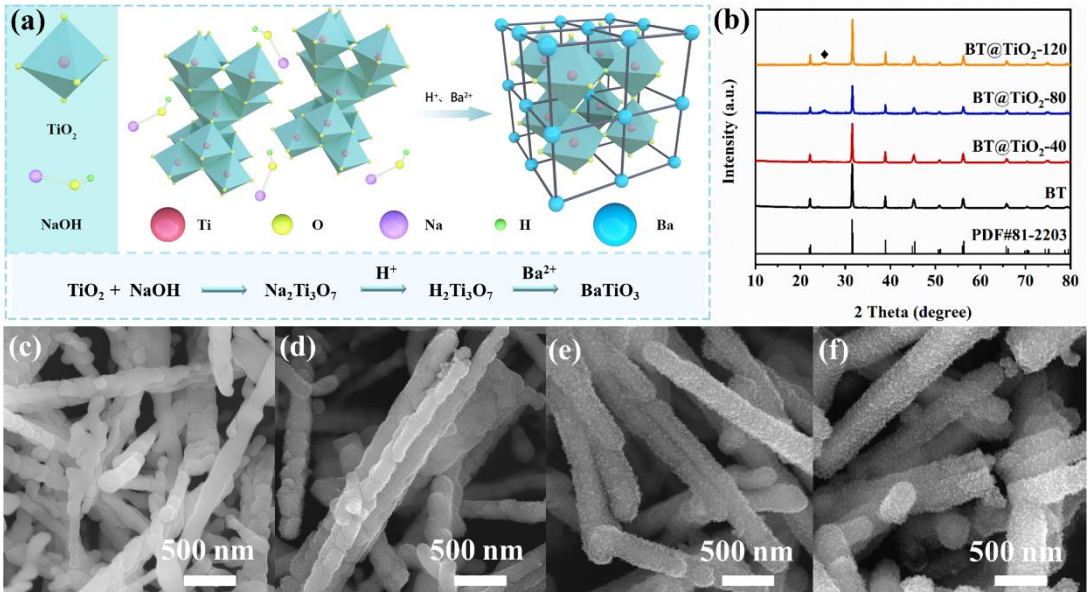

Fig. 1 (a) The flow chart of synthesis of $BaTiO_3$; (b) X-ray diffraction (XRD) patterns of BT and BT@TiO_2 samples, and SEM image of (c) BT NWs, (d) BT@TiO_2-40 NWs, (e) BT@TiO_2-80 NWs and (f) BT@TiO_2-120 NWs.

The thickness of the TiO_2 layer of BT@TiO_2 core-shell nanowire samples are measured by transmission electron microscopy (TEM) images (Fig. 2a-c). The outer surface of TiO_2 layers of BT@TiO_2-40, BT@TiO_2-80 and BT@TiO_2-120 NWs are approximately 10 nm, 45 nm and 55 nm, respectively. There corrospond to the size changes of nanowires in the SEM images. The partially enlarged high-resolution TEM (HRTEM) image confirms the co-existence of both phases in BT@TiO_2 sample (Fig. 2d). The lattice fringes with interlayer distance of 0.284 nm, which is marked by red lines, is corresponds to (101) crystal planes of tetragonal BT. In addition, a set of lattice fringes with spacing of 0.243 nm is distributed to (103) facet of anatase TiO_2 (marked with yellow line). The HRTEM spectras provide additional evidence to demonstrate that the phase stucture of the crystal. EDS mapping showed in Fig. 2e-g are conducted to further confirm the elements composition and distribution of the BT@TiO_2 nanowire. The signals of Ti, Ba and O elements are depicted in red, blue and green color, respectively.

The chemical states of the elements in BT@TiO_2 NWs are characterised by XPS measurements as Fig. 3 shows. In Fig. 3a, the peaks loacted at 780.10 eV and 795.42 eV are attributed to Ba atoms in the perovskite structure, corresponding to Ba 3d5/2 and Ba 3d3/2, respectively. The two slight bumps around 778.43 eV and 794.04 eV are assigned to Ba atoms in the non-perovskite structure [24]. In Fig. 3b, non-symmetric

peaks of 458.53 eV and 464.26 eV are typically assigned to the signals of Ti^{4+}, corresponding to Ti 2p3/2 and Ti 2p1/2 of BT@TiO_2, respectively [25]. In the spectrum of O 1s (Fig. 3c), only one peak located at 529.74 eV belongs to the signal of O 1s and no satellite peak indicates high crystallinity of BT@TiO_2 NWs. These observations substantiate the existence of Ba^{2+}, Ti^{4+} and O^{2-} in the BT@TiO_2 NWs.

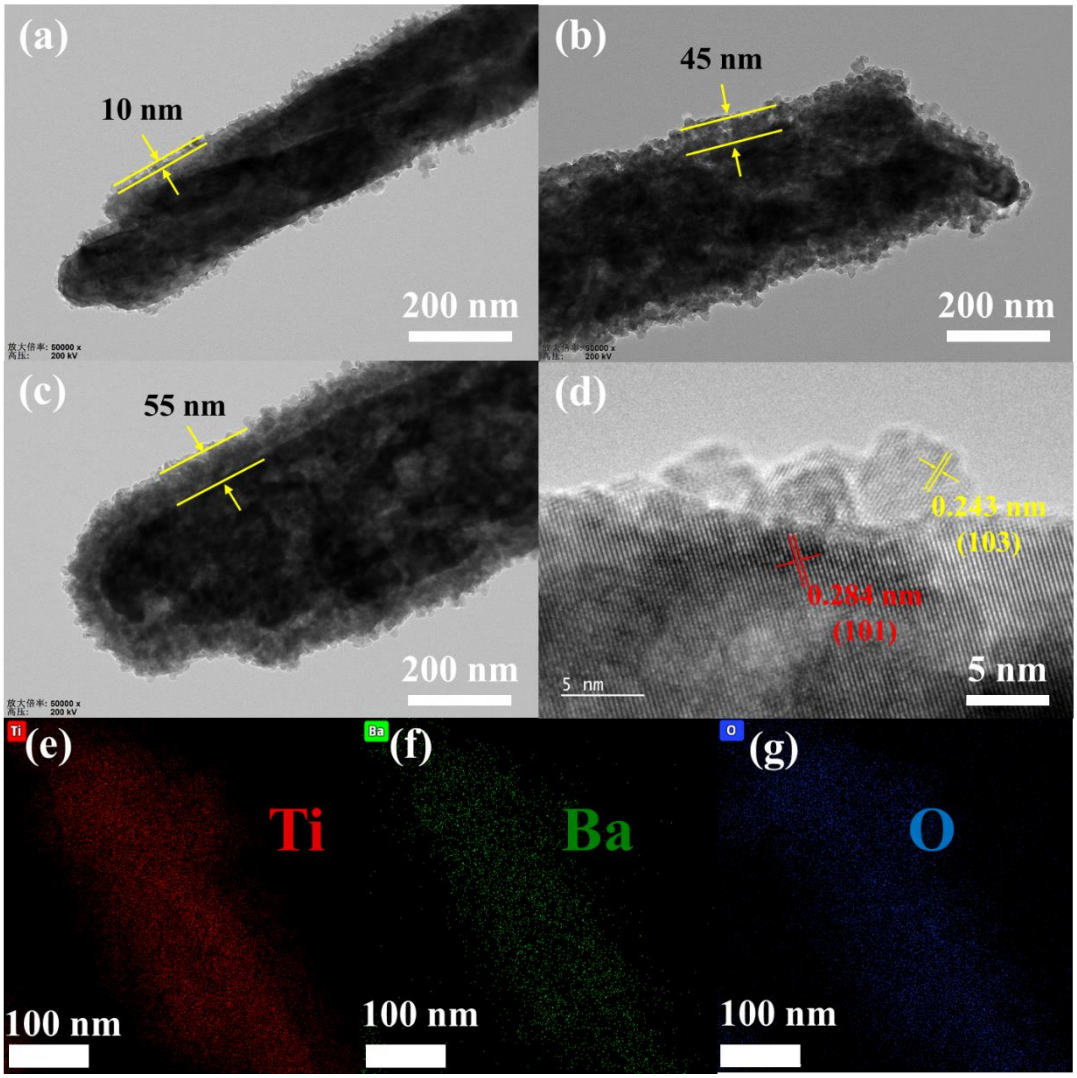

Fig. 2 TEM image of (a) BT@TiO_2-40 NWs, (b) BT@TiO_2-80 NWs and (c) BT@TiO_2-120 NWs; (d) HRTEM image of BT@TiO_2-40 NWs; EDS mapping images of BT@TiO_2-120 NWs as (e) Ti, (f) Ba and (g) O.

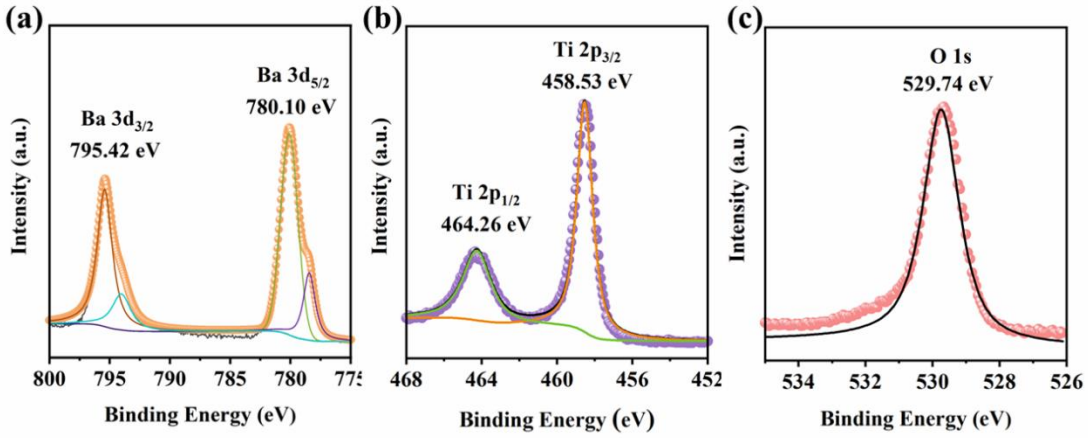

Fig. 3 High-resolution XPS spectra of (a) Ba 3d5/2 and Ba 3d3/2, (b) Ti 2p3/2 and Ti 2p1/2, and (c) O 1s in BT@TiO_2-120 NWs.

3.2 Catalytic performance and mechanism

As a general theory, the polarization phenomenon will be generated inside the piezoelectric material when the piezoelectric material is deformed by an external force in a certain direction [26]. At the same time, positive and negative charges will be generated on the opposite surfaces. The amount of charges is related to the deformation degree of piezoelectric material, and the deformation degree is related to the piezoelectric driving frequency, and load [27]. Therefore, in order to verify the effect of driving frequency on the piezoelectric catalytic performance of BT, 0.05 g BT is applied to degrade 5 mg/L RhB at 28, 45, 80 and 100 kHz, respectively. As Fig. 4a-c show, the degradation rate reached 89.3% in 30 min at ultrasonic frequency of 45 kHz, but only 17.1%, 5.84% and 3.87% at ultrasonic frequency of 28, 80 and 100 kHz, respectively. The first-order kinetic rate constant (*k)* is applied to reveal the degradation performance. As the following equation:

$$C = C_0 e^{-kt} \quad (1)$$

Where k can be calculated through the $\ln(C_0/C)$ - t plot. Fig. 4b and 4c clearly shows that the k of BT for 5 mg/L RhB degradation at 45 kHz is 0.08 min^{-1}, which is much higher than that at 28 kHz (0.007 min^{-1}), 80 kHz (0.002 min^{-1}) and 100 kHz (0.001 min^{-1}). This indicates that the ultrasonic frequency has a significant effect on the catalytic performance of piezoelectric materials. To further determine this effect and exclude the experimental randomness, the degradations of 10 mg/L RhB at 28, 45, 80 and 100 kHz are applied. The results still demonstrate that under a 45 kHz sonication frequency, the first-order kinetic rate constant reaches 0.018 min^{-1}, but only 0.006 min^{-1} at 28 kHz, 0.003 min^{-1} at 80 kHz and 0.001 min^{-1} at 100 kHz, respectively. The detailed degradation efficiency of RhB with different concentrations at different ultrasonic frequency is summarised in Table S1. This suggests that at a frequency of 45 kHz, BT has a higher piezoelectric catalytic performance than at 28/80/100 kHz, which supposed to be related to the reaction mode between the ultrasonic wave and liquid. Under the action of an ultrasonic wave, the liquid will produces ultrasonic cavitation [28, 29]. Water molecules will be deformed by pressure and lead to bubble formed. The implosion of bubble is caused by the compression, and the pressure at the moment of implosion can reach 10^8~10^9 Pa [30]. Stronger cavitation is more likely to be occurred under the low frequency. The liquid is subjected to a longer time interval of compression at low frequency, and the bubbles can grow to a larger size before implosion, which can increase the intensity of cavitation and the pressure of bursting is

increased [31, 32]. The increased pressure caused by the implosion of the bubbles can leads to a larger deformation of BT, which induced more polarization charges. In addition, Yang. et and Huang. et have also reported that a larger deformation can be achieved in materials forced at its resonant frequency[33, 34]. The piezoelectric catalytic performance of BT depends on the charge generated in the piezoelectric effect. Thus, the suitable ultrasonic frequency is necessary for achieving superior piezoelectric catalytic properties.

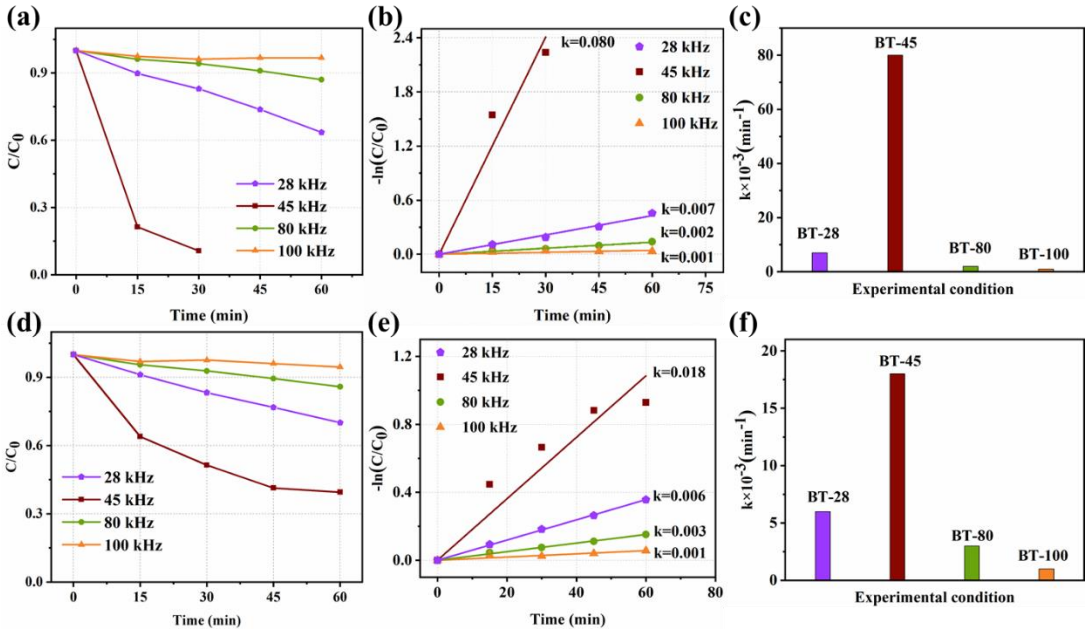

Fig. 4 Piezocatalytic activity of BT at different ultrasonic frequency as 28, 45, 80 and 100 kHz: (a) piezocatalytic degradation efficiency, (b) plots of ln(C_0/C)-vibration time and (c) rate constants k in the degradation of 5 mg/L RhB; (d)-(f) is the same to (a)-(c) but for the degradation of 10 mg/L RhB.

In order to clarify the operational principle of ultrasonic frequency in the piezoelectric catalysis process, FEM simulation with an applied force in a periodic function $y_{(force)}=F_1|\sin 2\pi t|$ (F_1=1 MPa, T=0.5 s), $y_{(force)}= F_1|\sin \pi t|$, ($F_1$=1 MPa, T=1 s)

and $y_{(force)}= F_2|\sin\pi t|$, ($F_2$ =2 MPa, T=1 s) are carried out as Fig. 5 shows. We have examined the piezoelectric potential distribution at several time points in the simulation process for analysis, and the whole simulation process is shown in the animation of the supporting material. From Fig. 5a to Fig. 5d, Fig. 5e to Fig. 5h and Fig. 5i to Fig. 5l, it can be concluded that the piezoelectric potential shows a regular periodic change with a periodic change of applied force. By comparing the half-period point as shown in Fig. 5a, Fig. 5f and Fig. 5j, the applied force is at a maximum for each periodic function model. This shows that when the applied force is the same (F_1=1 MPa), the generated piezoelectric potential does not change with frequency (T=0.5 s to T=1 s); and when the frequency is the same (T=1 s), the generated piezoelectric potential increases and increase of the applied force. For the same material, the generated electric potential is proportional to the amount of charge, thus we assumed that:

$$Q = \sigma U \tag{2}$$

Where Q presents the quantity of electric charge generated by the piezoelectric material, U is the generated piezoelectric potential, σ is a constant greater than zero. Therefore, the Q-t curve can be shown in Fig. 6a-c, and the area surrounded by the curve represents the total amount of charge generated in this period. The larger area contained in the curve means the sum of charge generated by the piezoelectric potential is greater. Taking 1s as an example, the area can be calculated with the following equation:

$$Q_1 = \sigma \times 2 \times F_1 \int_0^{0.5} sin2\pi t dt = 2kF_1 \tag{3}$$

$$Q_2 = \sigma \times F_1 \int_0^{1} sin\pi t dt = 2kF_1 \tag{4}$$

$$Q_3 = \sigma \times \mathrm{F}_2 \int_0^1 sin\pi t dt = 2kF_2 \quad (5)$$

For $F_2=2F_1$, therefore the $Q_3> Q_2= Q_1$. The simulation results verifies our proposal that the acoustic wave causes the bubble explosion in the solution through ultrasonic cavitation, and the bursting force of bubble causes the deformation of the piezoelectric material and generate a piezoelectric potential (and associated piezoelectric charges). The ultrasonic frequency affects the growth of bubble. With a lower frequency, the bubble can grow larger, and a larger bubble can generate a greater bursting force to the piezoelectric materials. However, the bubble does not grow indefinitely in the solution. When the period of ultrasonic wave is consistent with the time the bubble grows to the critical bursting point, the maximum piezoelectric potential and charge amount are generated at the corresponding ultrasonic frequency. On this basis, when the ultrasonic frequency is consistent with the resonant frequency of the piezoelectric materials, a lager deformation of the piezoelectric materials is achieved; while the period of ultrasonic wave is also have effect on the bubble blasting and leads to a superior deformation of materials. Therefore, the driving frequency has a significant effect on the piezoelectric catalytic performance for the combined effect of ultrasonic frequency on blasting force of bubbles and the resonance frequency of the materials itself.

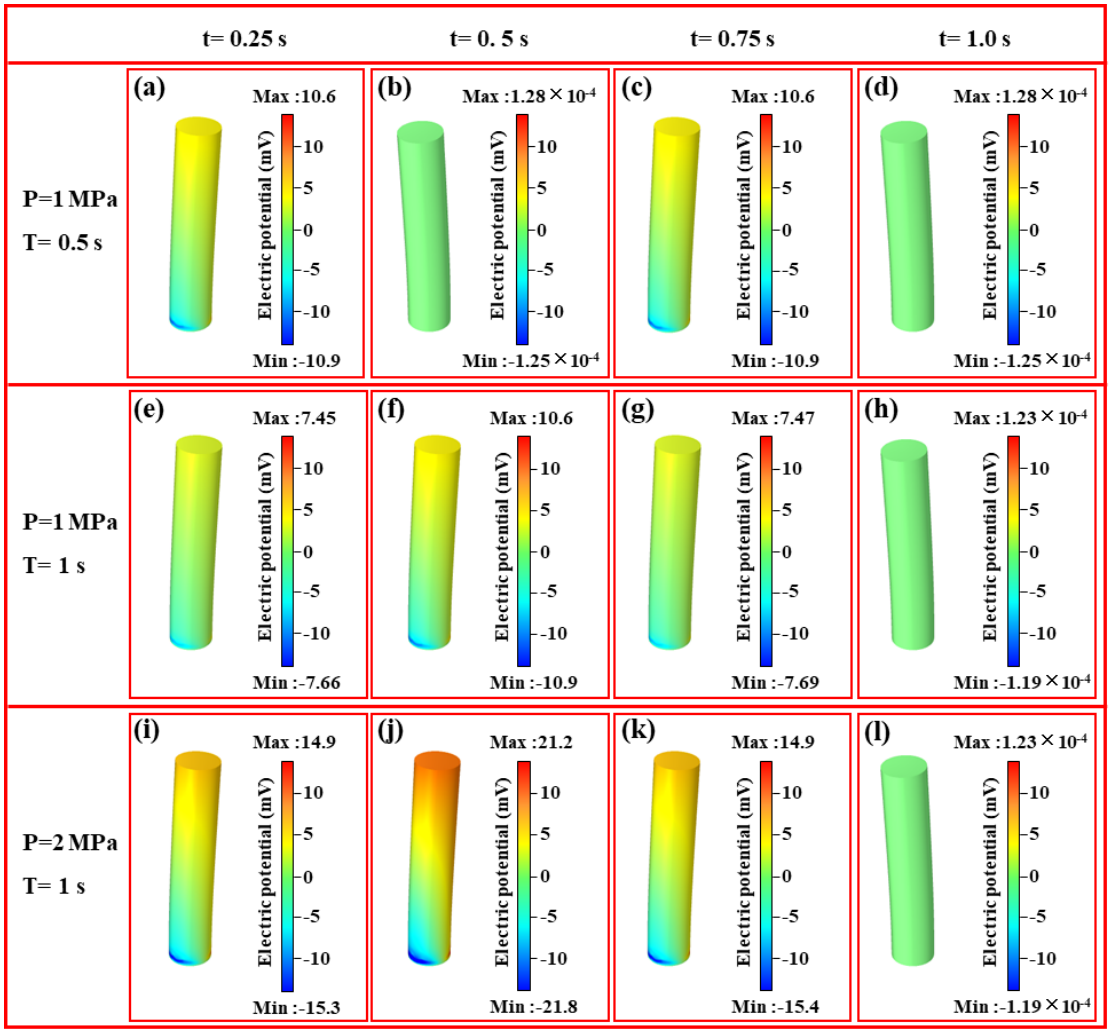

Fig. 5 FEM simulation to verify the effect of the frequency and magnitude of the applied force on the piezoelectric potential distribution in $BaTiO_3$. (a-d) the piezoelectric potential distribution in BT NW with an applied force in a periodic function $y_{(force)}=F_1|\sin 2\pi t|$, F_1=1 MPa, T=0.5 s, (a) t=0.25 s, (b) t=0.5 s, (c) t=0.75 s, (d) t=1.0 s; (e-h) the piezoelectric potential distribution in BT NW with an applied force in a periodic function $y_{(force)}= F_1|\sin \pi t|$, F_1=1 MPa, T=1 s, (e) t=0.25 s, (f) t=0.5 s, (g) t=0.75 s, (h) t=1.0 s; (i-l) the piezoelectric potential distribution in BT NW with an applied force in a periodic function $y_{(force)}= F_2|\sin \pi t|$, F_2 =2 MPa, T=1 s, (i) t=0.25 s, (j) t=0.5 s, (k) t=0.75 s, (l) t=1.0 s.

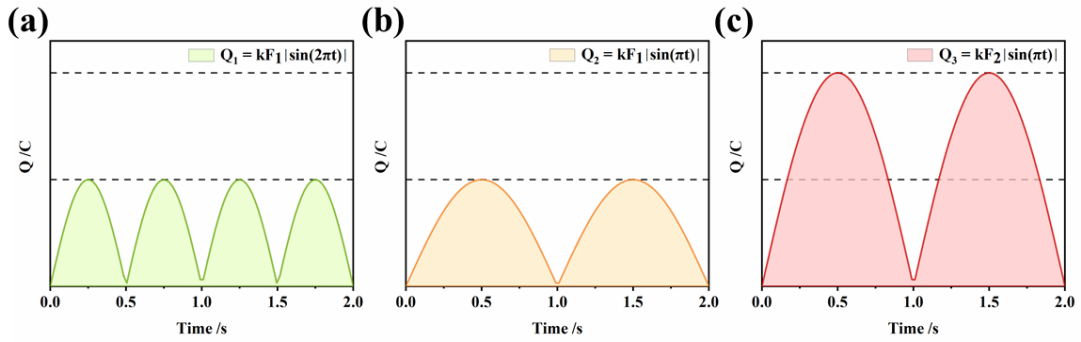

Fig. 6 The amount of charge produced by piezoelectric potential with the corresponding periodic function model in theory: (a) corresponding to periodic function $y_{(force)}=F_1|\sin 2\pi t|$; (b) corresponding to periodic function $y_{(force)}=F_1|\sin \pi t|$; (c) corresponding to periodic function $y_{(force)}=F_2|\sin \pi t|$.

Although the degradation performance with pure BT NWs has a good performance at low concentration of RhB (k=0.080 min^{-1} for 5 mg/L RhB), for high concentrations of dye such as 10 mg/L RhB the process remains inefficiency (k=0.018 min^{-1}). It is necessary to find a suitable and easy way to improve its catalytic performance for a high concentration dye. Thus 0.05 g BT, TiO_2, BT@TiO_2-40, BT@TiO_2-80 and BT@TiO_2-120 are applied to degrade 100 mL 10 mg/L RhB solution respectively with sonication and/or illumination. As shown in Fig. 7a-c, 98% RhB is degraded in 45 min in the presence of BT@TiO_2-80 or BT@TiO_2-120 catalyst with a rate constant of 0.086 min^{-1} and 0.089 min^{-1}, respectively. The BT@TiO_2-40 also exhibited relatively high piezo-photo-catalytic activity with 95.7 % of RhB degradation in 75 min and the rate constant is 0.042 min^{-1}. However, for the pure BT NWs and TiO_2, only 60.3% and 41.9% RhB is degraded in 75 min with the corresponding rate constant of 0.013 min^{-1} and 0.006 min^{-1}, respectively. In addition, the self-degradation efficiency of RhB is

negligible. The piezo-photo-catalytic activity of BT@TiO_2 outperformed that of pure BT NWs and TiO_2. In addition, when the layer thickness (TH) of TiO_2 increased, the catalytic performance was improved rapidly at first (i.e. TH=0 nm with k=0.013 min^{-1}, TH=10 nm with k=0.042 min^{-1} and TH= 45 nm with k=0.086 min^{-1}). Then, the rate of property enhancement slows when the thickness of the layer is further increased (TH=55 nm with k=0.089 min^{-1}). The introduction of TiO_2 will enhanced the number of charges excited by light absorption, and as more TiO_2 deposited, the more charges produced by light excitation. However, when the thickness of TiO_2 is large enough, the distance required for the charges transfer from bulk phase to surface to participate in the reaction is longer. Electrons and holes recombine in the bulk phase, and the effective charges for dye degradation will be reduced. Thus, there must be an appropriate thickness of TiO_2 for high catalytic performance of BT@TiO_2 core-shell structure. For the highest rate constant of 0.089 min^{-1} is contribute to BT@TiO_2-120 with the thickness of TiO_2 is 55 nm, BT@TiO_2-120 is applied to further study the mechanism of the coupling effect between piezo- and photo-catalysis.

In Fig. 7d-f, the piezo-photocatalytic degradation of 10 mg/L RhB has the best properties as compared to that of the sole piezocatalytic or photocatalytic process with 0.05 g BT@TiO_2-120 NWs. The degradation efficiency are 51.0%, 63.4% and 98.7% in 45 min for piezocatalytic alone, photocatalytic alone and combined piezo-photocatalytic respectively, corresponding to the rate constants of 0.016 min^{-1}, 0.023 min^{-1} and 0.095 min^{-1}, respectively. The rate constants of piezo-photocatalytic is much higher than that of the sum of piezocatalytic alone and photocatalytic alone, which

indicates the existence of strong coupling effects [35]. The mechanism of the coupling effect will be further analyzed in the following electrochemical characterization. In addition, the recyclability of BT@TiO_2-120 NWs for degrading RhB under co-effective of sonication and illumination is investigated as Fig. S1 shows. After six recycling experiments (since the recovered powder is insuffient to sustain the seventh recycling experiment), the changes of the degradation efficiency is negligible, which indicates the excellent stability of BT@TiO_2-120 NWs.

In order to gain a deeper understanding of the coupling mechanism, a study of the process of dye degradation is necessary. Several radical scavengers are added to clarify the role of free radicals plays in the catalytic oxidation process, as shown in Fig. 7g-i. Phenylhydrazine (BQ), ethylenediamine tetraacetate dehydrate (EDTA) and tert-butyl alcohol (TBA) are selected as $\bullet O_2^-$, h^+ and •OH scavengers, respectively. When BQ was added to the reaction system, the RhB degradation ratio decreased from 99.6% to 60.7% in 60 min with BT@TiO_2-120 NWs. While the addition of EDTA and TBA lead to relatively higher degradation ratios as 73.9% and 94.0% compared with the addition of BQ, respectively. The corresponding rate constants are 0.093 min^{-1}, 0.015 min^{-1}, 0.017 min^{-1} and 0.038 min^{-1} for no scavenger, BQ, EDTA and TBA added, respectively. The results indicate that with the sonication and illumination of BT@TiO_2-120 NWs produces abundant electrons and holes, as shown in Eq (6). The electrons and holes react with molecules of oxygen dissolved in the solution and water molecules as show in Eq (7) and Eq (8) and produces abundant $\bullet O_2^-$ radicals, slight h^+ and •OH radicals. It is worth noting that these scavengers are self-degraded under ultrasonic agitation,

especially for TBA molecules [24].

$$BT@TiO_2 + vibration + irradiation \rightarrow BT@TiO_2 (h^+ + e^-) \quad (6)$$

$$O_2 + e^- \rightarrow \bullet O_2^- \quad (7)$$

$$H_2O + h^+ \rightarrow \bullet OH + H^+ \quad (8)$$

Moreover, the active oxygen species (•OH and $\bullet O_2^-$) were further verified by the ESR technique as Fig. 7j and 7k shows. In Fig. 7j and 7k, three groups of obvious signals are generated with BT@TiO_2-120 NWs materials under (1) both light irradiation and ultrasonic vibration, (2) sole ultrasonic vibration and (3) sole light irradiation in RhB solution, respectively. However, without the BT@TiO_2-120 NWs materials, there almost no signal for (4) the pure RhB solution and (5) the pure DI water under both light irradiation and ultrasonic vibration, respectively. In addition, the intensities of ESR signals of both •OH and $\bullet O_2^-$ with BT@TiO_2-120 NWs materials under light irradiation and ultrasonic vibration (1) is stronger than that with only ultrasonic vibration (2) and light irradiation (3) in RhB solution. The above results confirm that •OH and $\bullet O_2^-$ active species are generated during the degradation process.

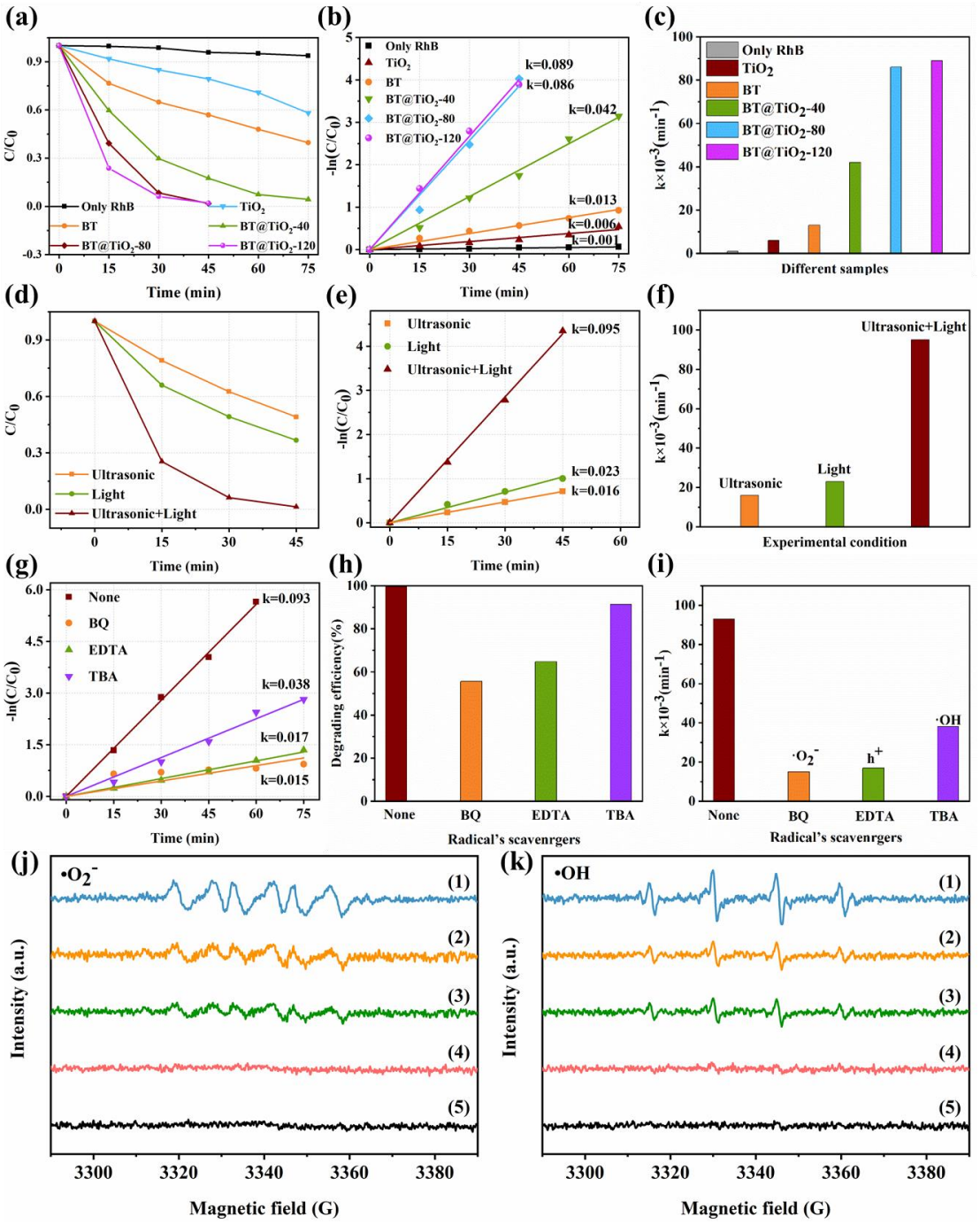

Fig. 7 (a) Piezophotocatalytic degradation efficiencies of 100 mL 10 mg/L RhB as a function of time with BT, TiO_2 and BT@TiO_2 samples; (b) their fitting kinetic curves and (c) the corresponding first order rate constants; (d) the degradation performance of RhB for the BT@TiO_2-120 through the piezo-catalysis, photo-catalysis and piezo-photocatalysis; (e) the fitting kinetic curves and (f) the corresponding first order rate

constants; (g) the fitting plot of $In(C/C_0)$ versus reaction time for piezophotocatalytic degradation of RhB with BT@TiO_2-120 in the presence of BQ, EDTA, TBA and blank for radical scavengers; (h) the corresponding degradation and (i) the corresponding first order rate constants; ESR of (j) $\bullet O_2^-$ and (k) •OH with radical spin-trapped by DMPO over (1) BT@TiO_2+RhB + Light + Ultrasonic, (2) BT@TiO_2+RhB + Ultrasonic, (3) BT@TiO_2+RhB + Light, (4) RhB + Light + Ultrasonic and (5) DI water + Light + Ultrasonic, respectively.

The electrochemical impedance spectra (EIS) shown in Fig. 8a aim to study the charge carrier transport properties of BT and BT@TiO_2-120 NWs. The smaller radius of Nyquist plot implies that the BT@TiO_2-120 NWs has a faster electron-hole pair separation rate and lower interfacial charge-transfer resistance. The pure BT NWs shows a larger radius compared with the BT@TiO_2-120 NWs, suggesting that the effective charges for catalytic reaction are decreased. Fig. 8b are Bode plots of both samples which is derived from the equivalent electric circuit of electrochemical impedance spectra (inner of Fig. 8b). The interface charge transfer resistance between the catalysis and the liquid is denoted as R_{ct}, and the high frequency region resistance of solution is denoted as R_s. The f_{max} value of BT and BT@TiO_2-120 NWs can be obtained from Bode plot which is 3.16 Hz and 2.61 Hz, respectively. The electron lifetime (s) can be calculated according to the following equation:

$$\tau = \frac{1}{2\pi f_{max}} \quad (9)$$

where f_{max} represents the highest frequency in Nyquist plots. The results are list at Table. 1, the electron lifetime is increased from 50.37 ms to 60.98 ms after coated with TiO_2.

This observation suggests that recombination of electrons and holes are inhibited for the heterojunction constructed from TiO_2 and BT, which provides a superior charge transfer capability of BT@TiO_2-120 NWs and achieved higher catalytic performance.

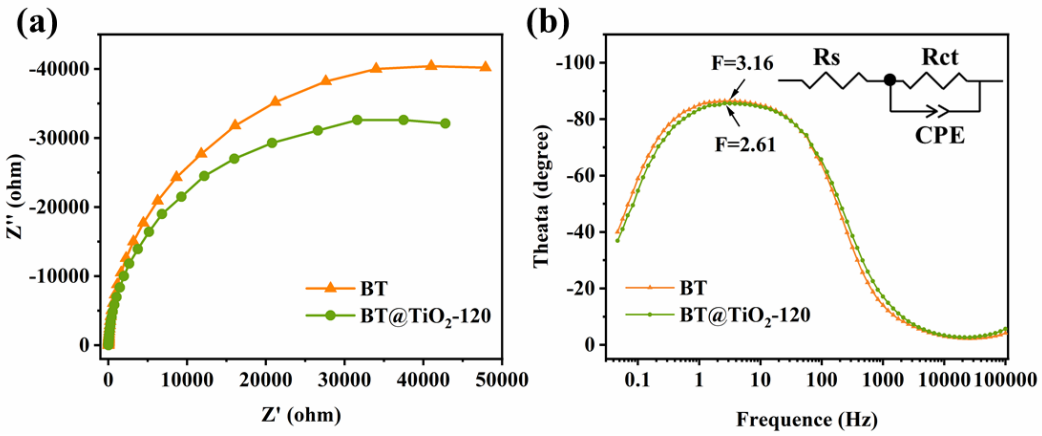

Fig. 8 (a) The EIS of BT and BT@TiO_2-120 NWs, (b) the corresponding Bode phase plots.

Table. 1 The electron lifetime (s) and the fitted parameters of BT and BT@TiO_2-120 NWs

Sample	**BT**	**BT@TiO_2-120**
Frequence/Hz	3.16	2.61
Time/ms	50.37	60.98
Rs/ohm	25.28	22.61
Rct/ohm	84662	69484

To further confirm the coupling effect caused by the heterojunction built at the interface of BT@TiO_2, UV-vis diffuse reflectance spectra of BT and BT@TiO_2-120 NWs are shown in Fig. 9a. The absorption of visible light has almost no change after being coated with TiO_2. The corresponding banding energy according to the equation

of $\alpha h\upsilon = B(h\upsilon - E_g)^{1/2}$ is show in Fig. 9b. The band gap of BT and BT@TiO_2-120 NWs are 3.21 eV and 3.19 eV. Mott-Schottky plots of BT and BT@TiO_2-120 NWs at different frequencies (i.e. 1000, 2000, and 3000 Hz, respectively) are shown in Fig. 9c-d, respectively. The positive slopes at various frequencies for BT and BT@TiO_2-120 NWs suggest they both are n-type semiconductors and electrons is the major carriers. That would explain the $\bullet O_2^-$ radicals produced by the piezophotocatalysis electrons and oxygen molecules are abundant, but not h^+ and •OH radicals. In addition, the flat band potential (V_{fb}) is determined by extrapolating the X-intercepts of the linear region in Mott-Schottky plots. The V_{fb} of BT is positive shifted from 0.12 eV to 0.16 eV after being coated with TiO_2, which mean the conduction band of BT and BT@TiO_2-120 NWs are ~0.22 eV and ~0.26 eV, while the valence band (VB) of BT and BT@TiO_2-120 NWs are ~−2.99 eV and ~−2.93 eV, respectively. The carrier concentration (*N*d) can be calculated using the slope with the following equation:

$$\frac{1}{Csc^2} = \frac{2}{\varepsilon\varepsilon_0 e_0 N_d}\left(U - V_{fb} - \frac{kT}{q}\right) \quad (10)$$

where e_0 is the electron charge; ε, ε_0 means the dielectric constant of BT and BT@TiO_2-120 NWs in a vacuum, respectively. As Fig. 9e shows, the slopes of Mott-Schottky plots of BT and BT@TiO_2-120 NWs at frequency of 1000 Hz are 20.64 and 14.14, the corresponding *N*d of BT and BT@TiO_2-120 NWs are 2.28×10^{17} cm^{-3} and 4.91×10^{18} cm^{-3}. The carrier concentration is increased by more than 20 times for the introduction of TiO_2, suggesting that the appropriate heterojunction plays an important role for suppressing electron-holes recombine. The linear sweep voltammetry (LSV) scans displayed in Fig. 9f further verify that the photocurrent density of pure BT is obviously

lower than that of BT@TiO_2-120 NWs under illumination. Thus, significant increase of carrier concentration is an important reason for the superior catalytic properties.

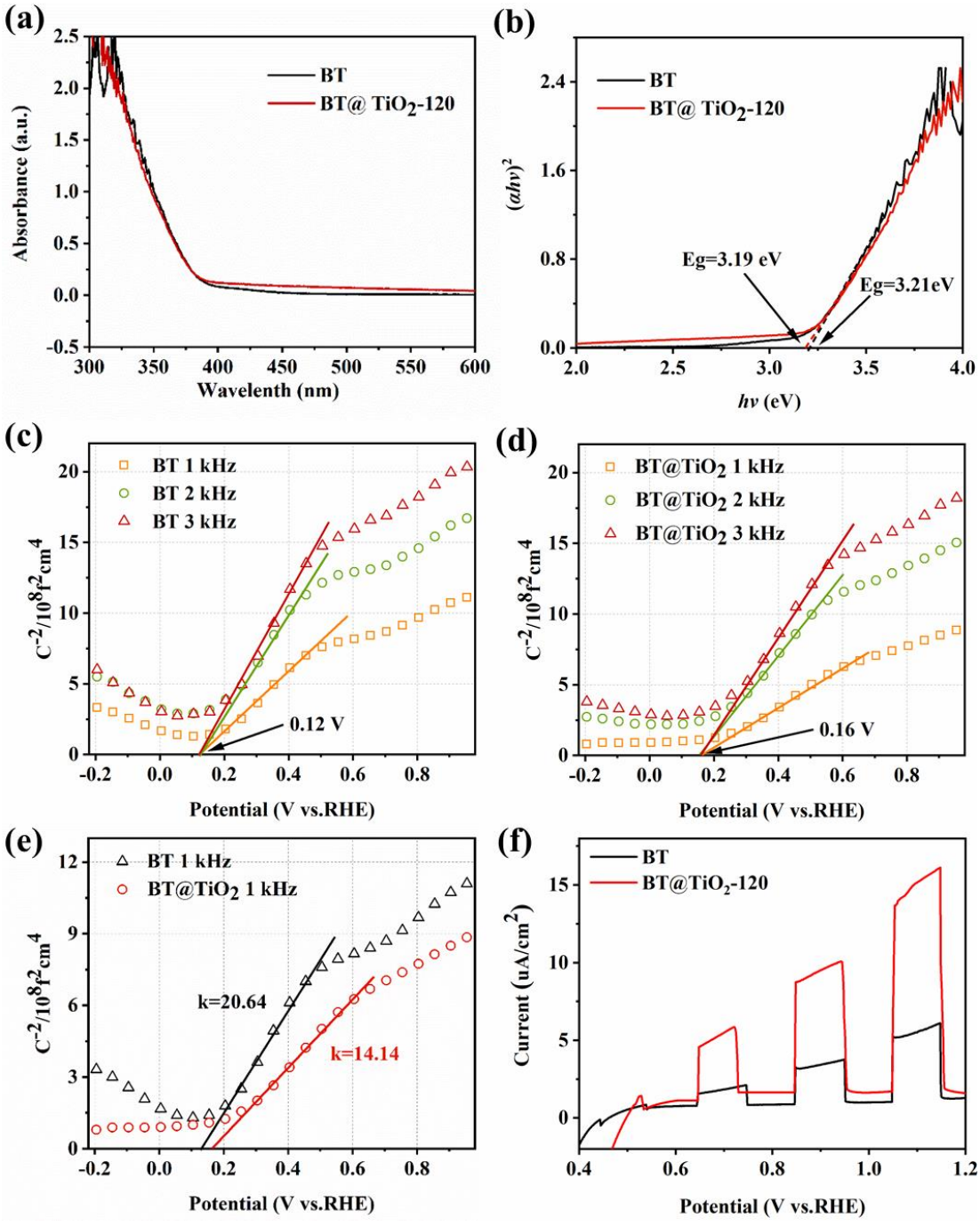

Fig. 9 (a) UV-Vis absorbance spectroscopy and (b) the corresponding banding energy of BT and BT@TiO_2-120 NWs; Mott-Schottky plots of (c) BT NWs and (d) BT@TiO_2-120 NWs at different frequencies; (e) Mott-Schottky plots of BT and BT@TiO_2-120

NWs at frequency of 1000 kHz; (f) linear sweep voltammetry scans of BT and BT@TiO_2-120 NWs under illumination/dark.

To summarise, the possible principle scheme of piezo-photoelectric synergy is shown in Fig. 10. In Fig. 10a, when BT is in contact with the solution, it is electrically neutral since the crystal structure does not change without external force, BT and the solution is in a state of static equilibrium. Under the action of ultrasonic wave, as Fig. 10b shows, the bubbles produced by ultrasonic cavitation exploded and a pressure is imposed on the BT. As a typical piezoelectric materials, asymmetric centers is produced for the lattice deformation of BT, and this leads to an internal polarization inside the BT.[36] Positive and negative charges will appear on the opposite surfaces of BT at the same time, and the band are tilted by the piezoelectric built in electric field [37-39]. Thus, the CB of BT can be more negative than the E (O_2/•O_2^-) = −0.33 V vs. NHE, and the VB of BT can be more positive than the E (OH^-/•OH) = 1.99 V vs. NHE [40]. This suggests that the electrons and holes can be successfully separated and participate in the catalytic reaction process in kinetics. In addition, the induced charge generated on the surface of the material will also react with the molecules or ions in the solution. Therefore, the piezoelectric catalytic degradation of dyes to be carried out. In Fig. 10c, after being coated with TiO_2, the photo-induced electrons are transferred to the CB and the heterojunction built by the BT@TiO_2 leads to a band bending on the surface of photocatalyst under illumination. The electrons on the CB of TiO_2 prefer to migrate to the CB of BT and then transfer to the surface to react with the active group in the

solution [41-43]. The existence of heterojunction can inhibit the recombination of charge, therefore the charge density and lifetime of BT@TiO_2 are improved in the electrochemical test compared with pure BT. However, the CB of the BT is more positive than E (O_2/•O_2^-), thus performance of dyes degradation with sole photocatalytic is inefficiency. Hence, the piezoelectric and photoelectric is combined to achieve efficient catalysis with coupling effect as shown in Fig. 10d. With the co-effects of sonication and illumination, the spontaneous polarization electric field is generated in BT, and the induced charge is generated on the surface of TiO_2, which leads to the band tilted in BT and band bending in TiO_2. The electrons can transfer from the negative CB to a relatively positive CB, in contrast, the holes are transferred from the positive VB to a relatively negative VB. It can be seen in Fig. 10d, the tilting and bending of the energy band caused by the introduction of piezoelectric polarization can lead to the perfect charge separation and the recombination of photoinduced charges in the bulk phase are inhibited [44-47]. Thus, the carrier intensity is increased, the lifetime of electron is longer and the catalytic properties is greatly improved.

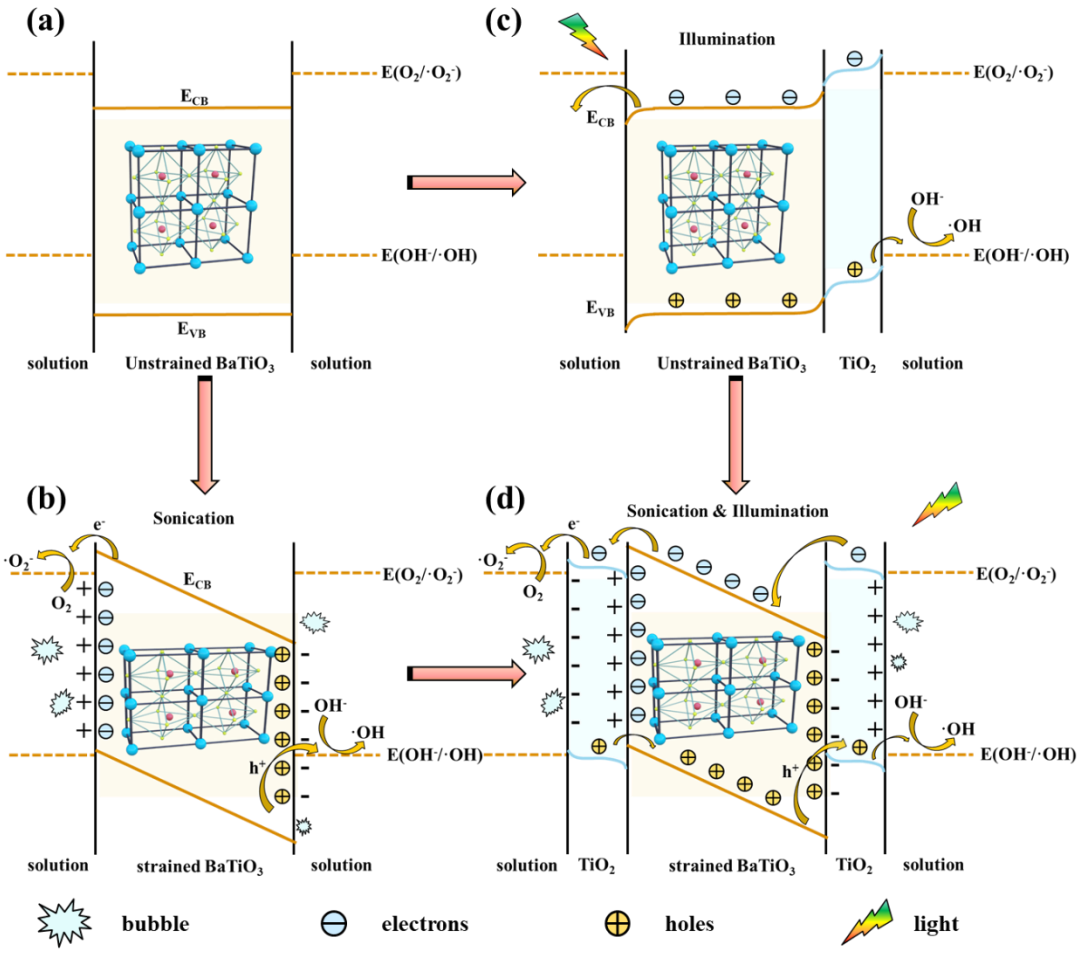

Fig. 10. Principle scheme of the piezocatalysis, photocatalysis and piezo-photocatalysis contains band tilting and surface reaction: (a) No obvious degradation can be observed without sonication and illumination; (b) BT with sonication only; (c) BT@TiO_2 with illumination only ; (d) BT@TiO_2 with sonication and illumination co-effective.

Given the excellent electrochemical properties (i.e. superior carrier concentration, high charge lifetime and lower conduction band), the coupling of BT and TiO_2 has great potential in piezophotocatalysis of high concentrated dye degradation, as show in Fig. 11. 100 mL 30 mg/L RhB, MB and IC are applied to detect the piezophotocatalysis performance with 0.05 g BT@TiO_2-120 NWs, respectively. Fig. 11a-c display the intensity of the absorbance spectra of dye in the degradation process. 99.5% RhB is

degraded in 75 min and the rose color notably disappears with RhB molecules is rapidly broken down over time. In Fig. 11b, the intensity of the absorption peak of MB decreases slowly compared with that of RhB with increasing degradation time. The degradation rate reaches 99.8% in 105 min, and the inset photograph of Fig. 11b shows color change in the process of MB degradation. In Fig. 11c, Indigo Carmine with a maximum absorption peak around 611 nm, is dramatically decreased with an increased reaction time. This exhibits the highest degradation rate among this three kinds of dyes with 99.7% of IC is degraded in 45 min. The initial deep indigo color of IC is rapidly faded with the increase of the time.

As can be seen in Fig. 11d-f, the kinetics of the degradation ratio and the fitting rate constant exhibits that the BT@TiO_2-120 NWs has an high piezophotocatalysis performance for high concentrated dye degradation. The rate constant reaches 0.067 min^{-1}, 0.047 min^{-1} and 0.108 min^{-1} for 30 mg/L RhB, MB and IC degradation with 0.05 g BT@TiO_2-120 NWs, respectively, which is higher than most of piezophotocatalysis reported before. Furthermore, 5 mg/L RhB is applied to degrade RhB with 0.05 g BT@TiO_2-120 NWs to compare with piezophotocatalysis previously reported. The results are shown in Fig.S2. The rate constant reaches 0.207 min^{-1} and 99.2% RhB is degraded in 30 min. The results of recent reports and this work are listed in Table 2. The *k* value of BT@TiO_2-120 NWs are superior to that of most reported piezoelectric materials (i.e. BT, ZnO [48], BNT, $BiFeO_3$ [49], $K_{0.5}Na_{0.5}TiO_3$ (KNN) and $KNbO_3$ and so on). The excellent piezo-photocatalytic activities caused by coupling effect may owning to the two reasons: (a) the heterojunction between TiO_2 and BT leads to superior

carrier concentration, higher charge lifetime and lower conduction band; (b) with the sonication of BT, the recombination of charge in bulk phase is inhibited by the electric field generated by the internal polarization.[50-52]

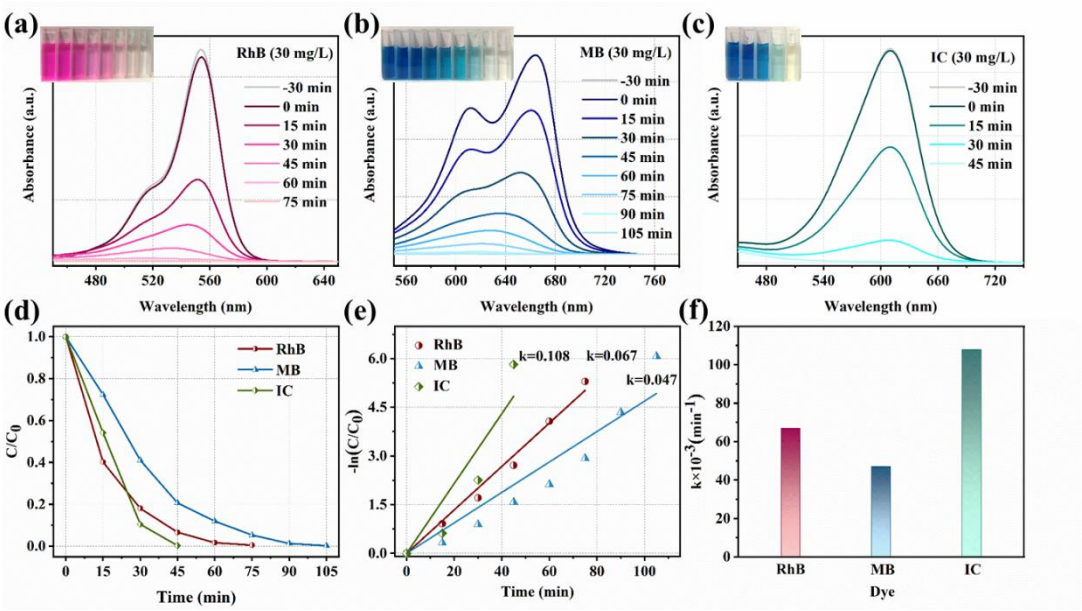

Fig. 11. Degradation of 30 mg/L (a) RhB, (b) MB and (c) IC with 0.05 g/L BT@TiO_2-120 NWs, respectively; (d) the corresponding degradation performance of dyes; (e) the fitting kinetic curves and (f) the first order rate constants.

Table 2 *k* values of recently reported piezocatalysts

Catalyst	$C_{(Catalyst)}$	$C_{(Dye)}$	Condition	year	$k\times10^{-3}$ (min^{-1})	Ref
BT nanowires	1.0 g/L	5 mg/ L MO	Ultrasonic: 40 kHz, 80 W	2018	~15	[30]
$ZnO/BaTiO_3$	1.0 g/L	10 mg/ L RhB	Ultrasonic: 40 kHz, 120 W Light: 100 mW cm^{-2}	2019	118	[24]

$KNbO_3$ nanosheets	0.5 g/L	10 mg/L RhB	Ultrasonic: 40 kHz, 110 W Light: 300 W	2019	22	[53]
$BiFeO_3/TiO_2$ nanoparticles	---	10 mg/L MV	Ultrasonic: 40 kHz, 300 W Light: 150W	2019	24	[54]
Li modified KNN nanoparticles	4.0 g/L	5 mg/L RhB	Ultrasonic: 40 kHz, 300 W	2020	25.16	[55]
BNT nanospheres	0.5 g/L	10 mg/L RhB	Ultrasonic: 40 kHz, 110 W Light: 200 mW cm^{-2}	2020	61	[56]
$BNT@TiO_2$ nanowires	0.5 g/L	10 mg/L RhB	Ultrasonic: 40 kHz, 100 W Light: 300 W	2020	27.9	[37]
BNT nanorods	1.0 g/L	5 mg/ L RhB	Ultrasonic: 28 kHz, 200 W Light: 300 w	2021	94	[57]
BNT nanorods	1.0 g/L	10 mg/L MB	Ultrasonic:28 kHz, 200 W Light: 300 w	2021	75	[57]
Ag deposited $BaTiO_3$	1.0 g/L	5 mg/L MB	Ultrasonic	2021	60.7	[9]
$BT@TiO_2$ nanowires	0.5 g/L	5 mg/L RhB	Ultrasonic:45 kHz, 200 W Light: 300 w		207	This work
$BT@TiO_2$ nanowires	0.5 g/L	30 mg/L RhB	Ultrasonic:45 kHz, 200 W Light: 300 w		67	This work

$BT@TiO_2$ nanowires	0.5 g/L	30 mg/L MB	Ultrasonic:45 kHz, 200 W Light: 300 w	47	This work
$BT@TiO_2$ nanowires	0.5 g/L	30 mg/L IC	Ultrasonic:45 kHz, 200 W Light: 300 w	108	This work

4. Conclusion

To summarize, the $BT@TiO_2$-120 NWs initiates high-efficiency piezo-photocatalytic properties with respect to degradation of high concentration dyes. The carrier concentration is increased from 2.28×10^{17} cm^{-3} to 4.91×10^{18} cm^{-3} and lifetime of charges is improved from 50.37 ms to 60.98 ms owing to the construction of a heterojunction between the TiO_2 and BT. Furthermore, the built-in electric field generated by the internal polarization of BT inhibits the recombination of charge in the bulk phase, resulting in the improvement of effective charges for catalytic reaction. With the coupling effect, the $BT@TiO_2$ has the almost highest rate constant as 0.207 min^{-1} for 5 mg/L RhB degradation, and exhibits the outstanding piezo-photocatalytic properties for high concentrated dye degradation.

Acknowledgement

This work was financially supported by National Key R&D Program of China (No. 2020YFA0711700), the National Natural Science Foundation of China (52002404, U19A2087), Hunan Natural Science Foundation (2019JJ40349), and the State Key Laboratory of Powder Metallurgy, Central South University, Changsha, China.

Reference 8 , 33 , 40

[1] K.K. Wang, Y. Liu, K. Kawashima, X.T. Yang, X. Yin, F.Q. Zhan, et al. Modulating charge transfer efficiency of hematite photoanode with hybrid dual-metal-organic frameworks for boosting photoelectrochemical water oxidation. Advanced Science. 2020;7(23):2002563.

[2] S. Li, Z.C. Zhao, J.Z. Zhao, Z.T. Zhang, X. Li, J.M. Zhang. Recent advances of ferro-, piezo-, and pyroelectric nanomaterials for catalytic applications. ACS Applied Nano Materials. 2020;3(2):1063-79.

[3] W.G. Tu, Y. Zhou, Z.G. Zou. Photocatalytic conversion of CO(2) into renewable hydrocarbon fuels: state-of-the-art accomplishment, challenges, and prospects. Adv Mater. 2014;26(27):4607-26.

[4] Y.C. Zhang, N.S. Afzal, L. Pan, X.W. Zhang, J.J. Zou. Structure-activity relationship of defective metal-based photocatalysts for water splitting: Experimental and theoretical perspectives. Advanced Science. 2019;6(10):1900053.

[5] V.S.R.K. Fang Han, Madapusi Srinivasan, Dharmarajan Rajarathnam, Ravi Naidu Tailored titanium dioxide photocatalysts for the degradation of organic dyes in wastewater treatment: A review. Applied Catalysis A-general. 2009;359:25-40.

[6] L. Han, F. Jing, J. zhang, X.Z. Luo, Y.L. Zhong, K. Wang, et al. Environment friendly and remarkably efficient photocatalytic hydrogen evolution based on metal organic framework derived hexagonal/cubic In_2O_3 phase-junction. Applied Catalysis B: Environmental. 2021;282:119602.

[7] T.M. Su, Z.Z. Qin, H.B. Ji, Y.X. Jiang, G. Huang. Recent advances in the

photocatalytic reduction of carbon dioxide. Environmental Chemistry Letters. 2015;14(1):99-112.

[8] W.Q. Qian, S.W. Xu, X.M. Zhang, C.B. Li, W.Y. Yang, C.R. Bowen, et al. Differences and similarities of photocatalysis and electrocatalysis in two-dimensional nanomaterials: strategies, traps, applications and challenges. Nano-Micro Letters. 2021;13(1):156.

[9] E.Z. Lin, Z.H. Kang, J. Wu, R. Huang, N. Qin, D.H. Bao. $BaTiO_3$ nanocubes/cuboids with selectively deposited Ag nanoparticles: Efficient piezocatalytic degradation and mechanism. Applied Catalysis B: Environmental. 2021;285:119823.

[10] M.Y. Wang, B. Wang, F. Huang, Z.Q. Lin. Enabling PIEZOpotential in PIEZOelectric semiconductors for enhanced catalytic activities. Angewandte Chemie International Edtion. 2019;58(23):7526-36.

[11] M.J. Dai, H.Y. Chen, F.K. Wang, Y.X. Hu, S. Wei, J. Zhang, et al. Robust piezo-phototronic effect in multilayer gamma-InSe for high-performance self-powered flexible photodetectors. ACS Nano. 2019;13(6):7291-9.

[12] Z.L. Wang. Piezotronic and piezophototronic effects. The Journal of Physical Chemistry Letters. 2010;1(9):1388-93.

[13] Q. Liu, Q. Hu, D. Zhai, Q.W. Sun, H. Luo, D. Zhang. Superior photo-piezoelectric catalytic performance using $Bi_{0.5}Na_{0.5}TiO_3$@$BiVO_4$ based cloth. Journal of Materials Chemistry A. 2021;9:17841-54.

[14] W. Lv, L.J. Kong, S.Y. Lan, J.X. Feng, Y. Xiong, S.H. Tian. Enhancement effect in

the piezoelectric degradation of organic pollutants by piezo-Fenton process. Journal of Chemical Technology & Biotechnology. 2017;92(1):152-6.

[15] J. Wang, Z.G. Xing, Z.L. Lu, K.N. Ding, H.D. Wang. First- principle study of the properties in $BaTiO_3$ and the electronic structure of H_2O adsorption on $BaTiO_3$. Int J Quantum Chem. 2020;121(8):121:e26576.

[16] A.A. Yadav, Y.M. Hunge, V.L. Mathe, S.B. Kulkarni. Photocatalytic degradation of salicylic acid using $BaTiO_3$ photocatalyst under ultraviolet light illumination. Journal of Materials Science: Materials in Electronics. 2018;29(17):15069-73.

[17] Fujishima A, H. K. Electrochemical photolysis of water at a semiconductor electrode. Nature. 1972;238(12):37-8.

[18] H.L. You, Z. Wu, Y.M. Jia, X.L. Xu, Y.T. Xia, Z.C. Han, et al. High-efficiency and mechano-/photo- bi-catalysis of piezoelectric-ZnO@ photoelectric-TiO_2 core-shell nanofibers for dye decomposition. Chemosphere. 2017;183:528-35.

[19] Q.Y. Li, R. Li, L.L. Zong, J.H. He, X.D. Wang, J.J. Yang. Photoelectrochemical and photocatalytic properties of Ag-loaded $BaTiO_3/TiO_2$ heterostructure nanotube arrays. Int J Hydrogen Energy. 2013;38(29):12977-83.

[20] C.Y. Xu, W.H. Huang, Z. Li, B.W. Deng, Y.W. Zhang, M.J. Ni, et al. Photothermal coupling factor achieving CO_2 reduction based on palladium-nanoparticle-loaded TiO_2. ACS Catalysis. 2018;8(7):6582-93.

[21] E.Z. Lin, N. Qin, J. Wu, B.W. Yuan, Z.H. Kang, D.H. Bao. $BaTiO_3$ nanosheets and caps grown on TiO_2 nanorod arrays as thin-film catalysts for piezocatalytic applications. ACS Applied Materials & Interfaces. 2020;12(12):14005-15.

[22] W.G. Yang, Y.H. Yu, M.B. Starr, X. Yin, Z.D. Li, A. Kvit, et al. Ferroelectric polarization-enhanced photoelectrochemical water splitting in TiO_2-$BaTiO_3$ core-shell nanowire photoanodes. Nano Lett. 2015;15(11):7574-80.

[23] S.-M. Jang, S.C. Yang. Highly piezoelectric $BaTiO_3$ nanorod bundle arrays using epitaxially grown TiO_2 nanomaterials. Nanotechnology. 2018;29(23):235602.

[24] X.F. Zhou, S.H. Wu, C.B. Li, F. Yan, H.R. Bai, B. Shen, et al. Piezophototronic effect in enhancing charge carrier separation and transfer in ZnO/$BaTiO_3$ heterostructures for high-efficiency catalytic oxidation. Nano Energy. 2019;66:104127.

[25] G.Q. Cao, N.A. Deskins, N. Yi. Carbon monoxide oxidation over copper and nitrogen modified titanium dioxide⋆. Applied Catalysis B: Environmental. 2021;285:119748.

[26] P.T. Thuy Phuong, Y. Zhang, N. Gathercole, H. Khanbareh, N.P. Hoang Duy, X.F. Zhou, et al. Demonstration of enhanced piezo-catalysis for hydrogen generation and water treatment at the ferroelectric curie temperature. iScience. 2020;23(5):101095.

[27] A. Koka, H.A. Sodano. A low-frequency energy harvester from ultralong, vertically aligned $BaTiO_3$ nanowire arrays. Advanced Energy Materials. 2014;4(11).

[28] M.E. Weber, W.Y. Chon. Distribution of ultrasonic cavitation intensities in a liquid system. The Canadian Journal of Chemical Engineering. 1967;45:238-40.

[29] Z.W. Liu, C.H. Ji, B. Wang, S.Q. Sun. Role of a nanoparticle on ultrasonic cavitation in nanofluids. Micro & Nano Letters. 2019;14(10):1041-5.

[30] J. Wu, N. Qin, D.H. Bao. Effective enhancement of piezocatalytic activity of $BaTiO_3$ nanowires under ultrasonic vibration. Nano Energy. 2018;45:44-51.

[31] L.Z. Ye, X.J. Zhu, Y. He, T.J. Song. Effect of frequency ratio and phase difference on the dynamic behavior of a cavitation bubble induced by dual-frequency ultrasound. Chemical Engineering and Processing - Process Intensification. 2021;165:108448.

[32] M. Ashokkumar, J. Lee, Y. Iida, K. Yasui, T. Kozuka, T. Tuziuti, et al. Spatial distribution of acoustic cavitation bubbles at different ultrasound frequencies. Chemphyschem. 2010;11(8):1680-4.

[33] W.Q. Qian, W.Y. Yang, Y. Zhang, C.R. Bowen, Y. Yang. Piezoelectric materials for controlling electro-chemical processes. Nano-Micro Letters. 2020;12(1):149.

[34] H.L. You, Z. Wu, L.H. Zhang, Y.R. Ying, Y. Liu, L.F. Fei, et al. Harvesting the vibration energy of $BiFeO_3$ nanosheets for hydrogen evolution. Angewandte Chemie International Edtion. 2019;58(34):11779-84.

[35] S. Xu, W. Qian, D. Zhang, X. Zhao, X. Zhang, C. Li, et al. A coupled photo-piezo-catalytic effect in a BST-PDMS porous foam for enhanced dye wastewater degradation. Nano Energy. 2020;77.

[36] L. Pan, S.C. Sun, Y. Chen, P.H. Wang, J.Y. Wang, X.W. Zhang, et al. Advances in piezo- phototronic effect enhanced photocatalysis and photoelectrocatalysis. Advanced Energy Materials. 2020;10(15).

[37] X.G. Xu, X.J. Lin, F.H. Yang, S.F. Huang, X. Cheng. Piezo-photocatalytic activity of $Bi_{0.5}Na_{0.5}TiO_3@TiO_2$ composite catalyst with heterojunction for degradation of organic dye molecule. The Journal of Physical Chemistry C. 2020;124(44):24126-34.

[38] Y. Liu, Y. Zhang, Q. Yang, S.M. Niu, Z.L. Wang. Fundamental theories of piezotronics and piezo-phototronics. Nano Energy. 2015;14:257-75.

[39] M.B. Starr, X.D. Wang. Fundamental analysis of piezocatalysis process on the surfaces of strained piezoelectric materials. Scientific Reports. 2013;3:2160.

[40] W. Qian, K. Zhao, D. Zhang, C.R. Bowen, Y. Wang, Y. Yang. Piezoelectric material-polymer composite porous foam for efficient dye degradation via the piezo-catalytic effect. ACS Applied Materials & Interfaces. 2019;11(31):27862-9.

[41] Y.P. Wang, X.F. Sun, T. Xian, G.R. Liu, H. Yang. Photocatalytic purification of simulated dye wastewater in different pH environments by using $BaTiO_3/Bi_2WO_6$ heterojunction photocatalysts. Opt Mater. 2021;113.

[42] X.D. Wang, G.S. Rohrer, H.X. Li. Piezotronic modulations in electro- and photochemical catalysis. MRS Bull. 2018;43(12):946-51.

[43] Y. Ma, P. Lv, F. Duan, J.L. Sheng, S.L. Lu, H. Zhu, et al. Direct Z-scheme $Bi_2S_3/BiFeO_3$ heterojunction nanofibers with enhanced photocatalytic activity. J Alloys Compd. 2020;834:155158.

[44] Y. Zhang, C.H. Liu, G.L. Zhu, X. Huang, W. Liu, W.G. Hu, et al. Piezotronic-effect-enhanced Ag_2S/ZnO photocatalyst for organic dye degradation. RSC Advances. 2017;7(76):48176-83.

[45] X. Yu, S. Wang, X.D. Zhang, A.h. Qi, X.R. Qiao, Z.R. Liu, et al. Heterostructured nanorod array with piezophototronic and plasmonic effect for photodynamic bacteria killing and wound healing. Nano Energy. 2018;46:29-38.

[46] X.Y. Xue, W.L. Zang, P. Deng, Q. Wang, L.L. Xing, Y. Zhang, et al. Piezo-potential enhanced photocatalytic degradation of organic dye using ZnO nanowires. Nano Energy. 2015;13:414-22.

[47] S. Singh, N. Khare. Coupling of piezoelectric, semiconducting and photoexcitation properties in $NaNbO_3$ nanostructures for controlling electrical transport: Realizing an efficient piezo-photoanode and piezo-photocatalyst. Nano Energy. 2017;38:335-41.

[48] Y. Chen, L. Wang, R.J. Gao, Y.C. Zhang, L. Pan, C.Y. Huang, et al. Polarization-enhanced direct Z-scheme ZnO-WO_{3-x} nanorod arrays for efficient piezoelectric-photoelectrochemical Water splitting. Applied Catalysis B: Environmental. 2019;259:118079.

[49] H.L. You, Z. Wu, L.H. Zhang, Y.R. Ying, Y. Liu, L.F. Fei, et al. Harvesting the vibration energy of $BiFeO_3$ nanosheets for hydrogen evolution. Angewandte Chemie International Edtion. 2019;58(34):11779-84.

[50] S.C. Tu, Y.X. Guo, Y.H. Zhang, C. Hu, T.R. Zhang, T.Y. Ma, et al. Piezocatalysis and piezo-photocatalysis: catalysts classification and modification strategy, reaction mechanism, and practical application. Adv Funct Mater. 2020;30(48):2005158.

[51] H.W. Huang, S.C. Tu, C. Zeng, T.R. Zhang, A.H. Reshak, Y.H. Zhang. Macroscopic polarization enhancement promoting photo- and piezoelectric-induced charge separation and molecular oxygen activation. Angewandte Chemie International Edtion. 2017;56(39):11860-4.

[52] Z. Liang, C.F. Yan, S. Rtimi, J. Bandara. Piezoelectric materials for catalytic/photocatalytic removal of pollutants: Recent advances and outlook. Applied Catalysis B: Environmental. 2019;241:256-69.

[53] D.F. Yu, Z.H. Liu, J.M. Zhang, S. Li, Z.C. Zhao, L.F. Zhu, et al. Enhanced catalytic performance by multi-field coupling in $KNbO_3$ nanostructures: Piezo-photocatalytic

and ferro-photoelectrochemical effects. Nano Energy. 2019;58:695-705.

[54] Y.L. Liu, J.M. Wu. Synergistically catalytic activities of $BiFeO_3/TiO_2$ core-shell nanocomposites for degradation of organic dye molecule through piezophototronic effect. Nano Energy. 2019;56:74-81.

[55] A. Zhang, Z.Y. Liu, B. Xie, J.S. Lu, K. Guo, S.M. Ke, et al. Vibration catalysis of eco-friendly $Na_{0.5}K_{0.5}NbO_3$-based piezoelectric: An efficient phase boundary catalyst. Applied Catalysis B: Environmental. 2020;279:119353.

[56] Z.C. Zhao, L.Y. Wei, S. Li, L.F. Zhu, Y.P. Su, Y. Liu, et al. Exclusive enhancement of catalytic activity in $Bi_{0.5}Na_{0.5}TiO_3$ nanostructures: new insights into the design of efficient piezocatalysts and piezo-photocatalysts. Journal of Materials Chemistry A. 2020;8(32):16238-45.

[57] X.F. Zhou, Q.W. Sun, D. Zhai, G.L. Xue, H. Luo, D. Zhang. Excellent catalytic performance of molten-salt-synthesized $Bi_{0.5}Na_{0.5}TiO_3$ nanorods by the piezo-phototronic coupling effect. Nano Energy. 2021;84:105936.